Chemical Geology 630 (2023) 121488

Contents lists available at ScienceDirect

Chemical Geology

journal homepage: www.elsevier.com/locate/chemgeo

Electrochemical reactions driving Mn-enrichment in Fe—Mn supergene ores: A mineralogical perspective

André Jorge Pinto [a,*], Nuria Sanchez-Pastor [b], Raul Santos Jorge [c]

[a] Departament of Geology, Faculty of Sciences, University of Oviedo, C/ Jesús Arias de Velasco, s/n, 33009 Oviedo, Spain
[b] Department of Mineralogy and Petrology, Faculty of Geological Sciences, University Complutense of Madrid, C/ José Antonio Novais, 12, Madrid 28040, Spain
[c] University of Lisbon, Faculty of Sciences, Dom Luiz Institute (IDL), Campo Grande, Ed. C6, 1749-016 Lisbon, Portugal

ARTICLE INFO

Editor: Marco Fiorentini

Keywords:
Manganese oxides
iron oxides
Supergene enrichment
Electrochemical reaction

ABSTRACT

Iron and manganese oxides embody a geochemical system of great environmental, biological, and economical relevance. Chemical equilibria and the stability of Fe—Mn phases under surface or near-surface conditions can influence the fate of contaminants in the environment, impact biological metabolic processes, or Fe and Mn phase distribution in weathered ores. In the present work, we focus on the textural, mineralogical, and chemical study of Fe—Mn ores from the weathered zone of a vein-hosted deposit outcropping in the Iberian Pyrite Belt, SW Portugal, by means of micro-Raman spectroscopy coupled with electron microprobe microanalysis. The aims of our investigation are i) identifying the several Fe and Mn phases occurring in differently enriched ores samples, ii) relating their chemical composition with possible mineralization mechanisms, and iii) defining the mineral paragenetic pathway related to the observed textural features. Our approach enabled both the identification of the coexisting Fe and Mn phases, and unravelling paragenetic pathways leading to supergene enrichment mineralizations. Collected evidence demonstrates that changes in Eh/*p*H can lead to goethite dissolution under reductive conditions, promoting the release of Fe^{2+} into solution, whose electrochemical interaction with Mn^{4+} results in the formation of several types of Mn oxides, and secondary goethite. Our data shows a clear relationship between the type of Mn oxide crystallized and the ratio of aqueous Mn^{3+}/Mn^{4+}, alongside other prevalent cations, incorporated into tunnel or interlayer structural sites, which may be also desorbed/solubilized from primary goethite.

1. Introduction

Iron and manganese are two elements of high industrial relevance, since they are essential to manufacture steel, a fundamental material for the development and sustenance of a modern industrialized society (Gutzmer and Beukes, 2009). Furthermore, manganese oxides offer applications in the manufacture of products such as batteries, insulators or ceramics (e.g. McBreen, 1975; Singh and Meenaloshini, 2008; Malinenko et al., 2013). Both elements may occur together in nature, due to their similar geochemical characteristics (Luo et al., 2018), commonly associated with the hydrothermal alteration and supergene enrichment processes, while minor deposits of magmatic and contact metamorphic origin also exist. Gutzmer and Beukes (2009) provide an extensive review of the most relevant mineralogical, geochemical, and economic aspects of iron and manganese ore deposits worldwide.

Iron and manganese oxides play an important role in the environmental fate and mobility of toxic metals and pollutants, due to their small particle size and high reactive surface, coupled with an Eh/*p*H-dependent high reactivity (e.g. Hochella et al., 2008; Zhao et al., 2012, etc.). For instance, the work of Rout et al. (2014), whose findings point towards a major effect of Mn incorporation over the adsorption capacity of goethite regarding metals such as Pb^{2+}, or Cd^{2+}, underlines the environmental relevance of the Fe and Mn system. The effectiveness of such adsorption reactions is related to oxide surface properties, whose variation can influence the solubility, toxicity and bioavailability of contaminants in soils and aquifers (e.g. Huang and Zhang, 2020; Taujale et al., 2016). Huang and Zhang (2020) analyzed the state-of-the art research concerning redox Fe and Mn oxide reactions in complex systems, with a special focus on arising environmental implications. There is also a link between manganese oxides and the biosphere, since many naturally occurring Mn oxides form through biologically mediated processes (Tebo et al., 2004; Santelli et al., 2011).

* Corresponding author.
E-mail addresses: jorgeandre@uniovi.es (A.J. Pinto), nsanchez@ucm.es (N. Sanchez-Pastor), rjorge@ciencias.ulisboa.pt (R.S. Jorge).

https://doi.org/10.1016/j.chemgeo.2023.121488
Received 6 February 2023; Received in revised form 17 March 2023; Accepted 13 April 2023
Available online 23 April 2023

The crystal chemistry of Mn oxides is particularly complex, stemming from the large variety of structural types and the non-stoichiometric features affecting natural mineralizations, when compared to ideal compositions. Moreover, natural manganese oxides frequently form masses of poorly crystalline materials, hard to distinguish both in the field and in hand specimens. Following on the footsteps of Bernardini et al. (2019), Post et al. (2020, 2021) provide a comprehensive Raman spectral analysis of tunnel and layer-structure manganese oxides, using both synthetic and natural specimens. Both investigations include insights on manganese oxidation states, structural and crystallographic peculiarities of Mn oxides, alongside their chemical compositions. This body of work provides a methodological pathway to interpret mineral paragenetic sequences when different types of Mn oxides and hydroxides are finely intergrown, enabling a more realistic approach when it comes to deciphering the physical-chemical governing factors of mineral evolution in these systems.

Previous researches on Fe—Mn ore mineralizations have focused especially on the characterization of oxide phases towards the establishment of broad metallogenetic models of iron and manganese deposition (e.g. Roy, 1981; Pracejus et al., 1988; Michailidis et al., 1997), leaving aside the chemical equilibria intricacies established among oxide phases, as reflected by textural features, commonly at the microscopic scale. In the present work, by means of micro-Raman spectroscopy coupled with electron microprobe microanalysis, we focus on the textural, mineralogical, and chemical study of Fe—Mn materials sampled from the weathered zone of a vein-hosted deposit (Serra da Mina, Iberian Pyrite Belt, SW Portugal). The aims of our investigation are i) identifying the several Fe and Mn phases occurring in differently enriched samples, ii) relating their chemical composition with possible mineralization mechanisms, and iii) defining the mineral paragenetic pathway related to the observed textural features.

2. Sample provenance and context

The present study focuses on the mineral paragenetic associations occurring in the weathered/enriched zone of the vein-hosted Fe—Mn deposit of Serra da Mina, SW Portugal. These mineralizations are included in the western portion of the Iberian Pyrite Belt, most specifically in the Cercal-Odemira sector, where a series of different types of Fe—Mn deposits occur. Despite its tonnage relevance (Carvalho et al., 1971), the mineralization processes related to Serra da Mina deposit are still poorly understood, with few recent literary references. Almeida (1945) proposes a primary mineralization of Fe and Mn carbonates, subsequently replaced by oxides of the same metals, by near surface, low-temperature processes. For the purposes of this research, the weathered/enriched zone of Serra da Mina deposit offers excellent examples of a large variety of Fe—Mn oxide mineralizations; a window opened towards the physical-chemical factors governing mineral nucleation and growth. The primary, vein-hosted mineralizations of this deposit consist of associations of hematite and goethite, with minor amounts of pyrolusite, quartz, and galena. Tectonic remobilization events, underpinning the polyphasic vein mineralization, lead to a secondary mineral paragenesis of goethite, hematite, pyrolusite, cryptomelane, manganomelane, and quartz. Continuous supergene enrichment over the latter ores yielded associations of goethite, pyrolusite, cryptomelane, coronadite, ramsdellite, manganomelane, quartz, and barite. The samples presently discussed originated from the latter ore zone, and a recent in depth characterization of Serra da Mina deposit is included in Santos (2020).

Fig. 1 displays images of hand-specimens of the two enriched materials sampled in this investigation, characteristic of the weathered section of the Serra da Mina deposit profile, including the geographical coordinates of sampling sites (World Geodetic System). Fig. 1a depicts sample CO-102, relative to a zone where a porous goethite and hematite thick layer is underlain by a fractured barite and quartz vein. Between these two layers, a darker, purplish stratum of Fe and Mn oxides occurs, also extending downwards, filling cracks and fractures within the vein. Fig. 1b corresponds to sample CO-79, also quite porous, comprising mostly acicular Fe oxides (goethite and hematite), finely intergrown with Mn-oxides, which also exist as geodes in cavities. The mineral grain size of sample CO-79 makes it impossible to identify the Mn phases present without the aid of a microscope.

3. Materials and methods

Selected samples of the two mineralogically distinct Mn-enriched zones, CO-102 and CO-79, collected at Serra da Mina site, were embedded in resin, polished, and studied with a petrographic microscope, under both transmitted and reflected light observation modes.

The Raman spectra of targeted phases were collected using a

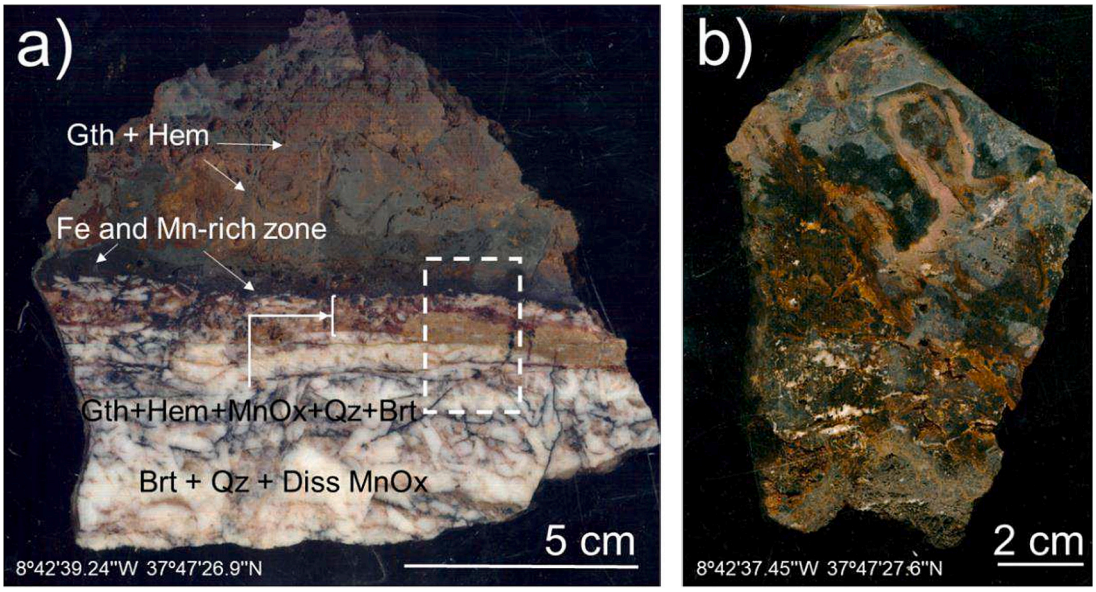

Fig. 1. Materials from the weathered-enriched zone of the Serra da Mina deposit, Iberian Pyrite Belt, SW Portugal; a) Sample CO-102, corresponding to less enriched materials, and b) sample CO-79, collected from the zone richer in Fe—Mn oxides. Geographical coordinates correspond to WGS84 system (*World Geodetic System*). Hem = Hematite, Gth = Goethite, Qz = Quartz, Brt = Barite, MnOx = Manganese oxides, Diss = disseminated.

confocal Thermo Fischer DXR Rama Microscope, with point-and-shoot capability and one micron of spatial resolution. A 10× magnification objective was employed alongside a 532 nm laser source of 10 mW at 100% power, but lower laser potency (<10 mW) was used for hydrated phases. The average spectral resolution of the Raman shift ranging from 70 to 3400 cm^{-1} was of 2–4 cm^{-1}, i.e. grating 900 lines/mm and a spot size of 2 μm. The system was operated under OMNIC 1.0 software, fitting working conditions such as pinhole aperture of 25 μm and bleaching time of 1–2 s; four exposures averaged in time of 12 s each.

Band component analysis was carried out using the software package "Fityk" (Wojdyr, 2010), which enables the analysis of Raman spectra by employing different fitting functions. Furthermore, the software allows the manipulation of specific parameters, such as band height, center, and half width at half maximum (hwhm).

After marking target zones for analysis, the polished thin sections were carbon coated prior to Electron Microprobe (EMP) determinations. The employed EMP was a JEOL Superprobe JXA-8900 M equipped with five WDS spectrometers, an EDS spectrometer, and a backscattered electron detector (BSE), enabling an on-session selection of the surfaces to be analyzed. Standard analyses applied 5 μm of beam diameter at a beam time current of 10 nA at 20 kV. Counting times on peaks and background ranged from 15 to 60s and 5 to 30s, respectively. The calculated detection limits were 208 ppm for Si and 108 ppm for Na (albite standard), 278 for Fe ppm and 312 ppm for Mn (almandine standard), 225 ppm for Ti, 153 ppm for Ca, and 133 ppm for Mg (kaersutite standard), 570 ppm for Zn (gahnite standard), 143 ppm for Al (sillimanite standards), 452 ppm for Ba (barite standard), 114 ppm for S and 165 for Pb (galena standard), 255 ppm for Sn (tin metal standard), 115 ppm for K (microcline standard), 293 ppm for Sr (strontianite standard) and 334 ppm for Ge (synthetic glass standard).

4. Results

4.1. Sample petrography

Fig. 2 displays reflected-light optical micrographs of the sampled mineralizations of Fe—Mn belonging to the enriched zone of the Serra da Mina deposit. Sample CO-102 (Fig. 2a) is characterized by the occurrence of goethite included in a pervasive mass of coronadite. Frequently, the latter exists in contact with fine-grained tabular goethite of a latter generation with respect to the massive one, as reflected by the texture displayed in Fig. 2b. Here, textural relationships between both types of goethite can be observed, depicting an anhedral grain of goethite with a rim of fine-grained tabular goethite, along a rough contact. Anhedral hematite also occurs scattered throughout the goethite materials, as well as anhedral to subhedral quartz grains. These mineralogical associations correspond to the Fe and Mn-enriched layer in sample CO-102, marked with a white circle in the thin-section image included in Fig. 2a, underlain by the barite and quartz vein with disseminated Mn-oxides, as depicted in Fig. 1a. Fig. 2c and d are referent to the mineralogical contents of sample CO-79, dominated by the paragenetic association of intergrown goethite and manganite, the latter occurring both as rosettes of prismatic crystals and anhedral masses (Fig. 2c). Fig. 2c and d are referent to the mineralogical contents of sample CO-79, dominated by the paragenetic association of intergrown goethite and manganite, the latter occurring both as rosettes of prismatic crystals and anhedral masses (Fig. 2c).

The porous nature of sample CO-79 is depicted in Fig. 2d, related to the tabular habit of individuals in the goethite matrix, within which large cavities appear lined with drusy growths of a hollandite-type phase, and filled with geodes of randomly oriented, prismatic chalcophanite crystals.

Deciphering the crystallization sequences mirrored by the textures encountered in both samples, as well as the physical-chemical governing mechanisms underpinning the implied enrichment process, entails

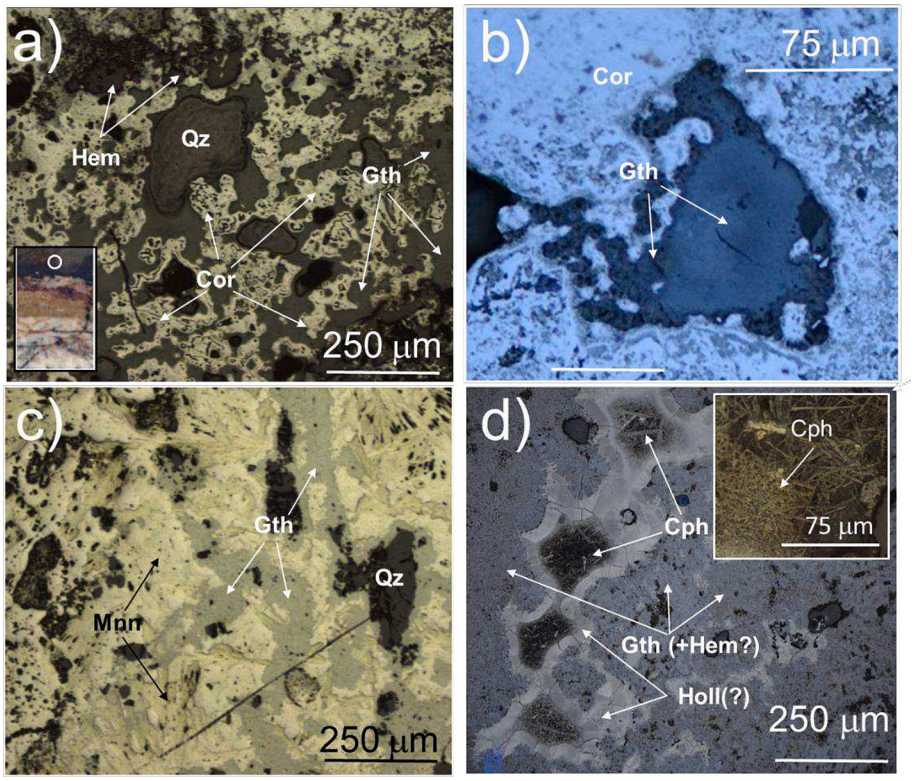

Fig. 2. Optical reflected-light micrographs under plane-polarized light of samples CO-102 (a, b), and CO-79 (c, d). Fig. 2b displays the textural relationship between two generations of goethite. Hem = Hematite, Cor = Coronadite, Gth = Goethite, Mnn = Manganite, Cph = Chalcophanite, Holl = Hollandite, Qz = Quartz.

investigating the structural and chemical subtleties of all observed phases; the object of the next sections.

4.2. Raman spectroscopy

Fig. 3 displays representative experimental Raman spectra, relative to Fe oxyhydroxide phases present in both CO-102 and 79 samples, focusing on the 150–750 cm^{-1} range, the most suitable shift interval to characterize such phases (Oh et al., 1998). No relevant differences were encountered between the Raman spectra of tabular individuals and their massive counterparts, i.e. the same set of bands were obtained, in spite of some shifts attributable to impurities and slight variations in chemical composition. The latter will be addressed in Section 4.3.

The spectrum of Fig. 3a, referent to the sample CO-102, reveals a set of 8 peaks in the vicinities of 161, 201, 241, 295, 392, 476, 545, and 681 cm^{-1} shifts. With the exception of the band at 161 cm^{-1}, all peaks can be ascribed to vibrational modes of the goethite (α-FeOOH) structure referenced in the scientific literature (i.e. Hanesch, 2009, Oh et al., 1998, De Faria et al., 1997, etc.), with the typical most intense peak at 392 cm^{-1} (this study) and a broad peak at 681 cm^{-1}. The peak at 161 cm^{-1} could be related to the incorporation of impurities into the structure of these phases, or as surface adsorbates. The spectra obtained for Fe oxyhydroxides in sample CO-79, exemplified in Fig. 3b, reveals a similar set of peaks (at cm^{-1} 167, 207, 301, 389, etc.), indicative of the presence of goethite. However, a second set around shifts of 227, 483, 512 and 613 cm^{-1} is also displayed, which can't be ascribed to such iron oxyhydroxide. The peak in the vicinities of 389 cm^{-1} reveals two bulges towards higher shift values, whose deconvolution displays a good level of fitting with the combination of bands at 403 and 416 cm^{-1}. These last, taken together with the aforementioned second set of peaks, are in good agreement with reference data regarding hematite (Fe_2O_3) (Hanesch, 2009, Oh et al., 1998, De Faria et al., 1997, etc.). Since a lower laser power was employed in measuring these phases, it is unlikely that hematite is the product of goethite dehydration during analytical procedures.

Figs. 4 and 5 display representative Raman spectra of tunnel-structure Mn oxides, focusing in the 200–800 cm^{-1} Raman shift range.

Fig. 4a, relative to sample CO-79, reveals a complex spectrum with a set of peaks at 270, 342376, 577, 629, and 747 cm^{-1} consistent with reference information regarding ramsdellite, MnO_2, (Post et al., 2020). Since this phase is isostructural with diaspore, crystallizing with space group *Pnma*, the resulting symmetry implies 18 Raman modes (Fateley et al., 1972), therefore explaining such spectral complexity. Furthermore, a second set of peaks at 398, 509, and 675 cm^{-1} is ascribable to the vibrational modes of a hollandite-group phase (Post et al., 2020). In such case, the peak at 629 cm^{-1}, could correspond to a composite band of $Mn^{4+/3+}$-O vibrational modes of both phases in that spectral region. Ramsdellite and hollandite-group minerals share important structural similarities (i.e. double chains of MnO_6 octahedra, forming structural tunnels), and therefore their topotactic intergrowth is a common feature. Fig. 4b, also relative to sample CO-79, depicts a Raman spectrum whose peaks at 264, 292, 383, 491, 530, 616 cm^{-1} are consistent with published data (Post et al., 2020) regarding manganite, MnOOH, with the exception of the band around 715 cm^{-1}. In fact, both spectra consistently display a band in the 710 cm^{-1} region, which allows speculating that another phase is responsible for it. The best candidate is ferrihydrite, $Fe_{10}O_{14}(OH)_2$, whose strong band in the mentioned region is still visible at moderate laser power (Hanesch, 2009). At instances, manganite spectra include a band around the 763 cm^{-1} region, which, given the common natural intergrowth of manganite with pyrolusite, MnO_2, could be most likely related to the latter phase. Since pyrolusite is isomorphic with rutile (TiO_2), and crystallizes with space group $P4_2/mnm$, three out of the arising four Raman-active phonon modes in the vicinities of 120, 535 and 665 cm^{-1} are largely overlapped by manganite bands in the same regions, resulting in a difficult spectral identification when the two phases are intergrown.

Fig. 5 shows representative Raman spectra relative to Hollandite-group phases in samples CO-102 and CO-79 (Fig. 5a and b, respectively). In each case, an inset depicting results in the 150–1300 cm^{-1} range is included, alongside the main spectral analysis focused in the 150/250–750 cm^{-1} interval. Both spectra show band associations, which are distinctive of hollandite-group minerals (Post et al., 2020), such as the MnO_6 octahedra vibrational modes at 505, 579 and 665 cm^{-1}, and 513, 576 and 635 cm^{-1}, for samples CO-102 and 79 respectively. Other bands reveal a good level of agreement with the reference information published by Post et al. (2020), such as the moderately intense band at 177 cm^{-1} (sample CO-102), and peaks at 399 and 382 cm^{-1} (samples CO-102 and 79, respectively). The undetermined band in the region of 715 cm^{-1} may be related to the presence of ferrihydrate, as previously described, and the bands in the 1320 cm^{-1} zone to either OH vibrational bending modes, related to OH^- groups with motion in the tunnel direction (Post et al., 2020), or a poorly crystalline hematite phase (Hanesch, 2009).

Peaks at 216 and 529 cm^{-1} in sample CO-102 could not be related to a specific phase. Hollandite group minerals are defined by the cation and water content included in tunnel positions and the corresponding electrostatic compensation by lower valence cations in the octahedral site, forming a complex solid solution system among multiple endmembers. Post et al. (2020) devised a correlation between the Mn—O stretching band in the 631 cm^{-1} region and the fraction of Mn^{3+} in the octahedral framework, associated with the Jahn-Teller distortion of the Mn-centered coordination polyhedra, given by the expression:

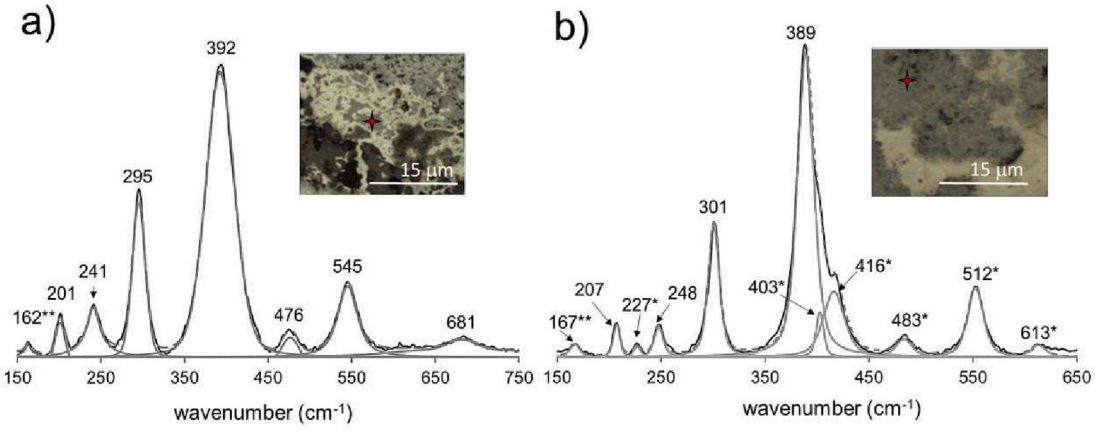

Fig. 3. Representative Raman spectra of a) goethite (sample CO-102) and b) intergrown goethite and hematite (sample CO-79). The inset micrographs depict the points of spectra acquisition. ** Non-ascribed peak, *Peaks ascribed to hematite vibrational modes.

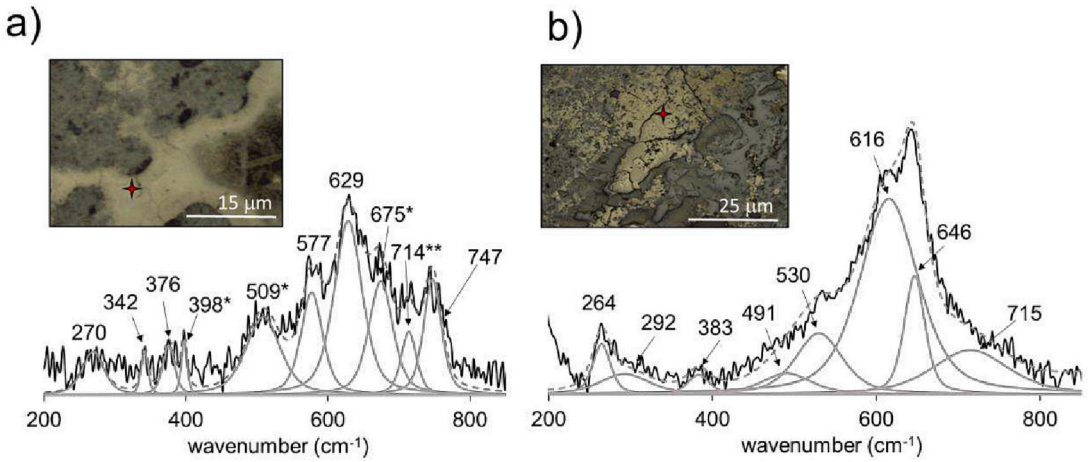

Fig. 4. Representative Raman spectra of a) ramsdellite and a hollandite-group phase, and b) manganite, both occurring in sample CO-79. The inset micrographs depict the points of spectra acquisition. ** Possible ferrihydrite, *Peaks ascribed to the vibrational modes of a hollandite-type structure.

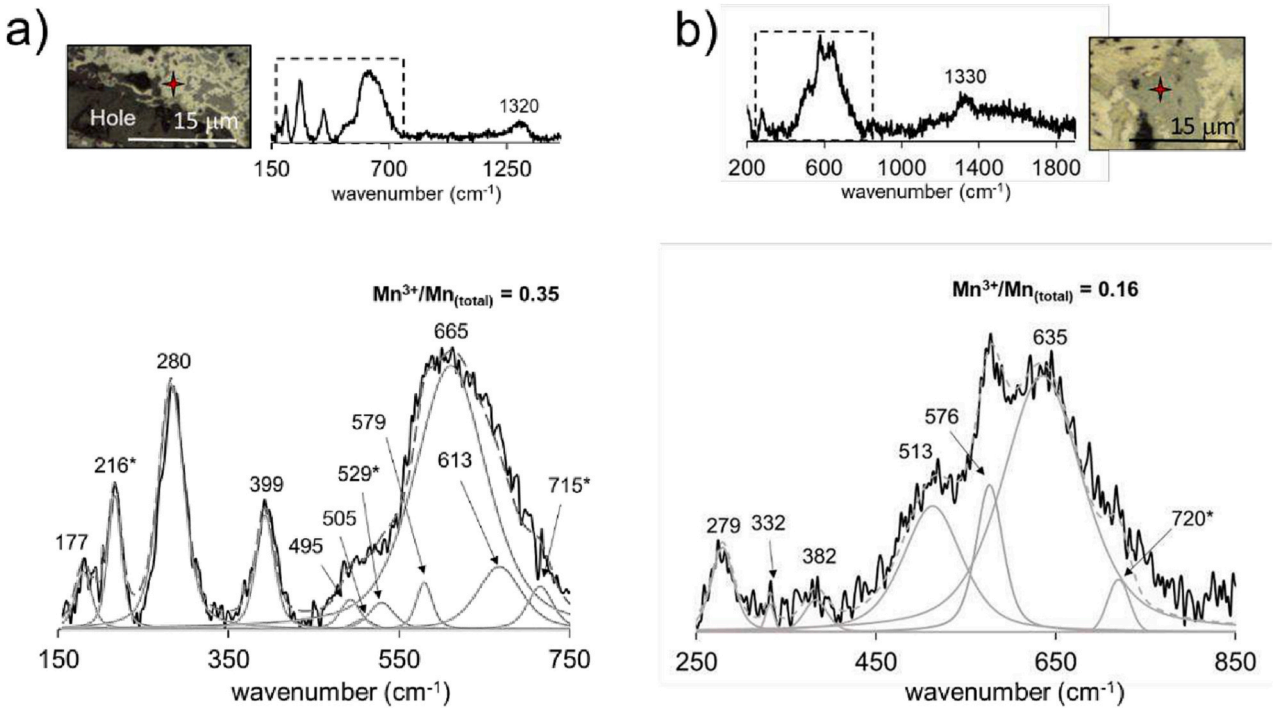

Fig. 5. Representative Raman spectra of a) hollandite-group phase in sample CO-102 with estimated $Mn^{3+}/Mn_{total} = 0.35$, and b) hollandite-group phase occurring in sample CO-79 with estimated $Mn^{3+}/Mn_{total} = 0.16$. The inset micrographs depict the points of spectra acquisition. * Non-ascribed bands.

$$Mn^{3+}/Mn_{total} = -0.0090499\nu_{max} + 5.9021 \quad (1)$$

where ν_{max} corresponds to the Raman shift in cm^{-1} of the Mn—O highest frequency mode. The application of this relationship to the obtained results reveals ratios of Mn^{3+}/Mn_{total} of 0.35 and 0.16 for samples CO-102 and CO-79, respectively. The former is close to values typical of coronadite, $Pb(Mn^{4+}, Mn^{3+})_8O_{16}nH_2O$, and hollandite, $Ba(Mn^{4+}, Mn^{3+})_8O_{16}nH_2O$, while the latter resembles the ratios found in cryptomelane, $K(Mn^{4+}, Mn^{3+})_8O_{16}nH_2O$, and manjiroite, $(K, Na)(Mn^{4+}, Mn^{3+})_8O_{16}nH_2O$. Further chemical definition of hollandite phases will be pursued in Section 4.3.

Fig. 6 displays an experimental Raman spectrum of prismatic, acicular crystals occurring as geodes in sample CO-79, optically identified as chalcophanite, $ZnMn_3O_7{\cdot}3H_2O$, focused in the 250–750 cm^{-1} spectral range. The obtained set of bands at 299, 378, 485, 512, 570, and 672 cm^{-1} are consistent with reference information regarding such phase (Post et al., 2021). The mode at 697 cm^{-1} corresponds to a bulge towards higher frequencies in the peak at 672 cm^{-1}, and could be the result of an adsorbed impurity. Similarly to hollandite group minerals, Post et al. (2021) found a correlation between the Raman frequencies of certain MnO_6 vibrational modes and the Mn^{3+}/Mn_{total} ratio for phyllomanganates. If nearly all Mn is tetravalent, the highest frequency modes related to internal MnO_6 octahedral vibrations should occur at higher wavenumbers in comparison to structures with some prevalence of Mn^{3+} in their composition. The correlation between the two parameters, defined by Post et al. (2021), is given by:

$$Mn^{3+}/Mn_{total} = -0.012034\nu_{max} + 8.0561 \quad (2)$$

In the present case, the calculated value ($Mn^{3+}/Mn_{total} \sim -0.03$) is close to zero, pointing towards either chalcophanite or rancieite,

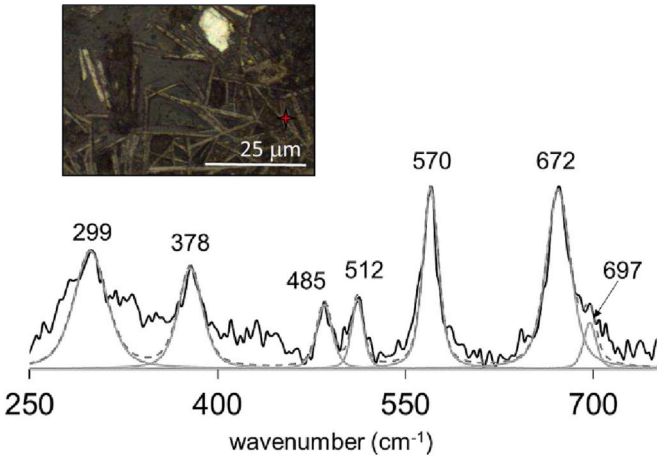

Fig. 6. Representative Raman spectra of chalcophanite occurring in geodes in sample CO-79. The inset micrographs depict the point of spectra acquisition.

$CaMn_3O_7{\cdot}3H_2O$. Nevertheless, the occurrence of well-defined spectral bands, uncharacteristic of rancieite (Post et al., 2021), seem to confirm the identity of chalcophanite. Chemical analysis included in the following section will contribute in settling this matter.

4.3. Chemical characterization Fe and Mn phases

Table 1 displays representative analysis of the different kinds of goethite encountered in samples CO-102 (1–3) and CO-79 (4 and 5), with atomic fractions based in two oxygen atoms per unit formula.

Results obtained for goethites in sample CO-102 all yield formulas close to $(Fe^{3+}, Al^{3+}\ Mn^{4+}, Zn^{2+}, Pb^{2+})_{\Sigma=0.8–0.9}O_{1+x}OH_{1–2x}$, whose stoichiometric deviations from an ideal formula can be ascribed to adjustments in the O^{-2}/OH^{-} ratio to compensate the incorporation of cations with different valence. A similar crystal-chemical feature has been invoked to explain the chemical composition of yellow ochre by Clark and Curri (1998), latter related by Hanesch (2009) with the degree of crystallinity of goethite. Goethites of sample CO-79 also reveal such slight deviation from an ideal stoichiometry, with formula $Fe_{1.3}OOH$.

Goethite in sample CO-102 occurs as minor amounts of massive anhedral mineralizations (analysis 1) and more frequently as latter generation fine-grained aggregates of tabular individuals (analyses 2 and 3). Despite sharing similar structural formulas, noticeable variations exist regarding the concentration of Zn, which in tabular goethites is nearly two-fold as concentrated as in massive ones. Tabular goethites occurring in coronadite-rich zones (3) have lower Pb concentrations that those formed in areas with less coronadite (2). All goethite in sample CO-79 forms a fine-grained matrix of tabular crystals, of which high and low Zn varieties occur (analyses 4 and 5, respectively). The overall compositions of goethites in samples CO-102 and CO-79 reveal higher contents of both Pb and Zn in the former, showing approximately the double concentration of Zn regarding CO-79, which merely contains trace amounts of Pb.

Table 2 illustrates representative analysis of the pervasive hollandite-group phase present in sample CO-102, whose optical characteristic and Raman spectral features pointed towards coronadite. Here, the highest concentrated divalent cation is Pb^{2+}, which further confirms such identification, and therefore the calculated atomic fractions are based on 16 oxygen per unit formula. Analyses (1) and (2) are referent to coronadite in the goethite-bearing matrix, and sparsely disseminated in barite veins, respectively. The determined formulas are very similar for both instances, conforming to $(Pb^{2+}, Zn^{2+}, Ba^{+}, Na^{+}, K^{+})_{\Sigma=1.08–1.11}(Mn^{4+}, Mn^{3+}\ Al^{3+}, Fe^{3+})_{\Sigma=6.88–7.29}\ (O, OH)_{16}nH_2O$. Deviations from the ideal stoichiometry can be related to the replacement of octahedral O^{2-} for OH^{-}, to compensate the existence of both mono and divalent cations in the tunnel sites (Post et al., 2020). Finally, only slight chemical differences exist between the two modes of occurrence, namely a slightly higher content in Pb and lower Mn in coronadite associated with Fe oxyhydroxides.

Table 3 refers to representative chemical analyses of Mn oxides occurring in sample CO-79, namely ramsdellite (1), chalcophanite (2), and cryptomelane (3). Analysis (1) reflects a hydrated ramdsellite composition, with formula $(Mn^{4+}, Fe^{3+}, Al^{3+})_{\Sigma=0.82}(O, OH)_2$. The results listed in analysis (2) are relative to prismatic crystals of chalcophanite occurring in geodes, therefore with atomic fractions based in 10 oxygen per unit formula. According to Post and Appleman (1988), Mn^{2+} may occur in the interlayer site of chalcophanite, which in the present case, after filling the octahedral MnO_6 position, yields a formula $(Zn^{2+}, Fe^{2+}, Mn^{2+})_{\Sigma=1.12}Mn_3^{4+}O_7{\cdot}2.82H_2O$. The occurrence of similarly peculiar stoichiometries and their relationships with structural deviations from an ideal chalcophanite is discussed in Michailidis et al. (1997).

Table 1
Chemical analysis of goethites from Serra da Mina deposit: *(1)–(3)* sample CO-102 and *(4)–(5)* sample CO-79. The atomic fractions were determined according to 2 oxygen per unit formula. *Expressed as total iron, **Calculated by difference of weight percent, b.d. = below detection.

	(1)	*(2)*	*(3)*	*(4)*	*(5)*
Al_2O_3	0.3	0.5	0.7	0.1	0.2
Na_2O	0.2	0.2	0.2	0.1	<0.1
MnO	1.5	2.6	1.1	0.2	0.6
MgO	<0.1	<0.1	<0.1	<0.1	<0.1
Fe_2O_3O*	79.0	74.1	76.3	79.5	80.4
PbO	1.8	1.3	0.6	<0.1	<0.1
ZnO	1.7	3.2	3.2	1.4	0.7
SO_3	0.6	b.d.	0.3	0.1	0.1
SiO_2	b.d.	b.d.	b.d.	1.7	1.4
H_2O**	15.2	18.0	17.6	16.9	16.6
Total	84.8	82.0	82.4	83.1	83.4
Al	<0.1	<0.1	<0.1	<0.01	<0,01
Na	<0.01	<0.01	<0.1	<0.01	<0.01
Mn	<0.1	<0.1	<0.1	<0.01	0.01
Mg	<0.001	<0.001	<0.001	<0.001	<0.01
Fe^{3+}	0.8	0.7	0.8	1.3	1.3
Pb	<0.1	<0.01	<0.01	<0.001	<0.001
Zn	<0.1	<0.1	<0.01	0.02	0.01
S	<0.1	–	<0.01	<0.01	<0.01
Si	–	–	–	<0.1	<0.1

Table 2
Chemical analysis of coronadite from Serra da Mina deposit occurring in sample CO-102. The atomic fractions were determined according to 16 oxygen per unit formula. *Expressed as total iron, **Calculated by difference of weight percent, b.d. = below detection.

	(1)	*(2)*
Al_2O_3	0.7	0.1
BaO	0.2	0.5
K_2O	<0.1	0.1
Na_2O	<0.1	0.5
MnO	53.3	58.6
TiO_2	b.d.	–
Fe_2O_3*	4.4	0.3
CaO	<0.1	–
PbO	26.1	21.6
ZnO	0.3	0.4
H_2O**	14.8	17.8
Total	85.2	82.3
Al	0.1	<0.1
Ba	<0.1	<0.1
K	<0.1	<0.1
Na	<0.1	0.1
Mn	6.7	6.8
Fe^{3+}	0.5	<0.1
Ca	<0.01	<0.01
Pb	1.0	0.8
Zn	<0.1	<0.1

Table 3
Chemical analysis of *(1)* ramsdellite, *(2)* chalcophanite and *(3)* cryptomelane from Serra da Mina deposit occurring in sample CO-79. The atomic fractions were determined according to 2, 10 and 16 oxygen per unit formula for analysis *(1)*, *(2)* and *(3)*, respectively. *Expressed as total iron, **Calculated by difference of weight percent, b.d. = below detection.

	(1)	*(2)*	*(3)*
Al_2O_3	0.7	0.2	0.4
BaO	0.3	0.2	0.6
K_2O	0.3	1.9	3.0
Na_2O	0.2	0.9	0.6
MnO	71.9	58.5	70.4
TiO_2	<0,1	b.d.	–
MgO	<0,1	0.2	0.0
Fe_2O_3*	1.8	–	–
FeO*	–	1.2	2.0
CaO	<0.1	<0.1	0.2
PbO	b.d.	b.d.	<0.1
ZnO	0.5	12.0	0.8
SO_3	<0.1	<0.1	<0.1
SiO_2	0.2	0.2	0.1
H_2O**	24.0	24.5	22.0
Total	76.2	75.5	78.0
Al	<0.01	<0.1	<0.1
Ba	<0.01	<0.1	<0.1
K	<0.01	<0.1	0.4
Na	<0.01	<0.1	0.1
Mn	0.8	3.4	6.8
Ti	<0.001	–	–
Mg	<0.001	<0.1	<0.001
Fe^{3+}	<0.001	–	–
Fe^{2+}	–	0.1	0.2
Ca	<0.1	<0.1	<0.1
Pb	–	–	<0.01
Zn	<0.01	0.6	<0.1
S	<0.001	<0.1	<0.01
Si	<0.01	<0.1	<0.1

Analysis (3) is relative to the hollandite-group phase found lining the inner walls of chalcophanite-bearing cavities, whose formula based in 16 oxygen reveals a non-stoichiometric solid, closer to the cryptomelane (i.e. K-rich) endmember. Such formula corresponds to $(K^+, Na^+, Ba^{2+}, Ca^{2+}, Mg^{2+}, Zn^{2+})_{\Sigma=0.70}(Mn^{4+}, Mn^{3+}\ Al^{3+}, Fe^{3+})_{\Sigma=7.05}\ (O, OH)_{16}nH_2O$.

The finely intergrown character of manganite and pyrolusite made it impossible to obtain reliable analysis of each phase, especially considering their very similar chemical contents.

Table 4 includes the detailed structural formulas of all analyzed phases for each sample, alongside with the mineral mode of occurrence.

5. Discussion

5.1. Goethite dissolution and variations in cation content

The textures of goethite mineralizations observed in sample CO-102 strongly suggest the occurrence of two separate nucleation events yielding the formation of Fe-oxyhydroxide. The earliest one involved the formation of massive, anhedral goethite – volumetrically less prevalent in the sample – followed by the formation of tabular, fine-grained goethite, surrounding, and replacing earlier goethite. Sample CO-79 only reveals goethite crystallized in the latter mode of occurrence. These paragenetic relationships point towards changes in the physical-chemical environment (i.e. lower *p*H, reducing conditions), leading to the destabilization of earlier goethite and its dissolution, with the consequent release of its chemical contents to the aqueous phase. Favorable physical-chemical circumstances, to be discussed in Section 5.2, resulted in the crystallization of a second-generation goethite alongside Mn oxides. A clear correlation exists between the cationic contents of second-generation goethites and the type of co-crystalized Mn oxide. For instance, in sample CO-102, abundant in coronadite (a Pb-bearing Mn oxide), tabular goethites exhibit lower Pb contents than

Table 4
Summary of phase formulas determined from EMP analyses. The acronym *n.s.* refers to 'non-stoichiometric'.

Sample	*Phase*	*Mode of occurrence*	*Formula*
102	Goethite	Massive, anhedral	$(Fe^{3+}_{0.82}, Al^{3+}_{0.01}, Mn^{4+}_{0.02}, Zn^{2+}_{0.02}, Pb^{2+}_{0.01})_{\Sigma=0.88}O_{1+x}OH_{1-2x}$
		Tabular, coronadite-rich zone	$(Fe^{3+}_{0.70}, Al^{3+}_{0.01}, Mn^{4+}_{0.03}, Zn^{2+}_{0.03}, Pb^{2+}_{0.005})_{\Sigma=0.78}O_{1+x}OH_{1-2x}$
		Tabular, coronadite-poor zone	$(Fe^{3+}_{0.80}, Al^{3+}_{0.01}, Mn^{4+}_{0.01}, Zn^{2+}_{0.03}, Pb^{2+}_{0.002})_{\Sigma=0.85}O_{1+x}OH_{1-2x}$
	Coronadite	Fe oxyhydroxide matrix	$(Pb^{2+}_{1.04}, Zn^{2+}_{0.03}, Ba^{+}_{0.01}, Na^{+}_{0.01}, K^{+}_{0.01})_{\Sigma=1.1}(Mn^{total}_{6.69}, Al^{3+}_{0.12}, Fe^{3+}_{0.49})_{\Sigma=7.3}(O, OH)_{16}nH_2O$
		Disseminated in barite veinlets	$(Pb^{2+}_{0.80}, Zn^{2+}_{0.04}, Ba^{+}_{0.03}, Na^{+}_{0.14}, K^{+}_{0.02})_{\Sigma=1.03}(Mn^{total}_{6.82}, Al^{3+}_{0.02}, Fe^{3+}_{0.03})_{\Sigma=6.87}(O, OH)_{16}nH_2O$
79	Goethite	Tabular, higher Zn	$(Fe^{3+}_{1.30}, Zn^{2+}_{0.02})_{\Sigma=1.32}\ O_{1+x}OH_{1-2x}$
		Tabular, lower Zn	$(Fe^{3+}_{1.30}, Zn^{2+}_{0.01})_{\Sigma=1.31}O_{1+x}OH_{1-2x}$
	Ramsdellite	Anhedral, drusy	$(Mn^{4+}_{0.80}, Fe^{3+}_{0.009}, Al^{3+}_{0.006})_{\Sigma=0.82}(O, OH)_2$
	Cryptomelane, *n.s.*	Anhedral, drusy	$(K^{+}_{0.44}, Na^{+}_{0.14}, Ba^{2+}_{0.03}, Ca^{2+}_{0.02}, Mg^{2+}_{0.006}, Zn^{2+}_{0.06})_{\Sigma=0.70}(Mn^{total}_{6.84}, Al^{3+}_{0.05}, Fe^{3+}_{0.17})_{\Sigma=7.06}(O, OH)_{16}nH_2O.$
	Chalcophanite	Prismatic, geodes in cavities	$(Zn^{2+}_{0.6}, Fe^{2+}_{0.1}, Mn^{2+}_{0.4})_{\Sigma=1.11}Mn^{4+}_3O_7 2.82H_2O$

their earlier-formed massive counterparts. Fig. 7a) and b) display the variations of Zn and Pb, respectively, as a function of Mn in all analyzed goethites of samples CO-102 and CO-79, expressed as weight percent of cation oxide. Sample CO-79 comprises exclusively second-generation tabular goethites, whose compositions in Zn^{2+} and Pb^{2+} are strikingly lower than goethites in sample CO-102, regardless of occurrence mode. Furthermore, a closer inspection shows that sample CO-79 is also richer in Mn oxides, both volumetrically and in structural variety (i.e. layered and tunnel-structure Mn oxides). It is possible, then, to conclude in favor of a solution-mediated concentration and transfer of cationic content from primary, massive goethites to a cohort of Mn oxides, of which sample CO-79 represents a more advanced stage, accompanied by the formation of secondary goethite.

Such process of progressive dissolution of iron oxide coupled with re-precipitation of solute contents in secondary Fe—Mn ores amounts to supergene enrichment, a mechanism mirrored by the highest dispersion of Zn and Pb concentrations in goethites occurring in sample CO-102, when compared to CO-79.

5.2. Mn oxide paragenetic sequence

The paragenetic sequence relating the formation of a second generation of goethite and manganese oxides is necessarily controlled by redox reactions taking place between aqueous Fe and Mn. An acidic and low fO_2 aqueous solution could lead to dissolution of primary goethite, and the release of its chemical content into the fluid (Michailidis et al., 1997). Under such conditions, the presence of aqueous Fe^{2+} is favored. If there is also Mn^{4+}present in the system (for instance in the form of an oxide), at 25 °C and room pressure, the electrochemical exchange established between the two ions results in the oxidation of iron to Fe^{3+} and reduction of manganese to Mn^{3+}, in response to the more positive standard redox potential (E^0) of the Mn^{4+} in MnO_2, according to the half-equations:

$$Fe^{3+}{}_{(aq)} + e^- \leftrightarrow Fe^{2+}{}_{(aq)}, E^0 = 0.77\ v \quad (3)$$

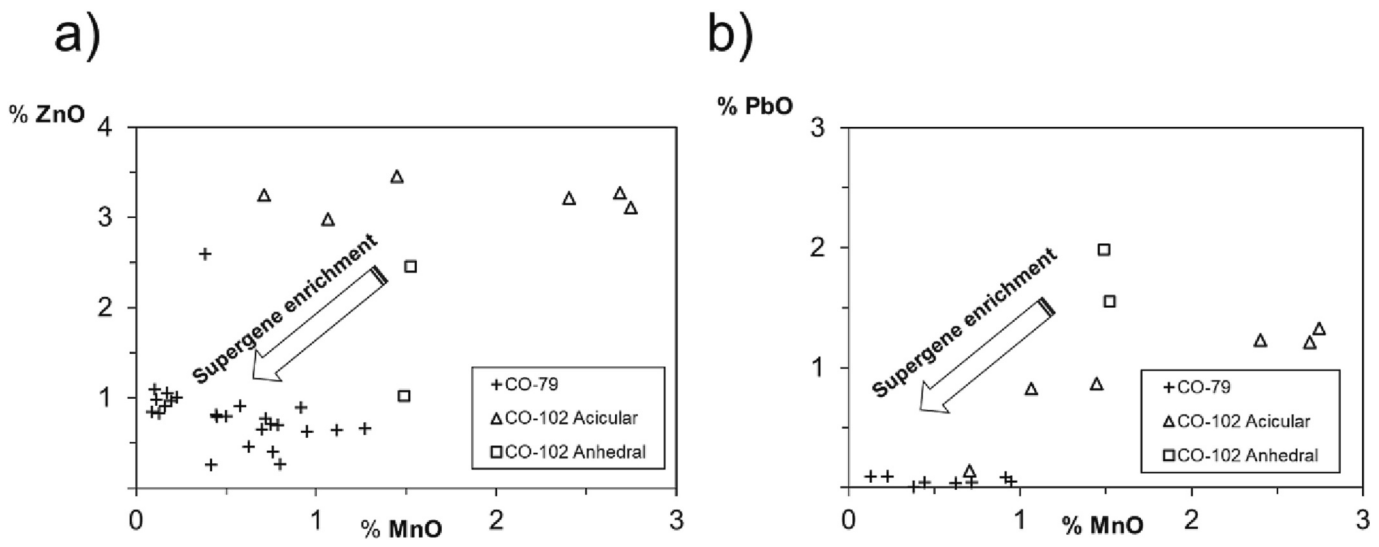

Fig. 7. a) ZnO and, b) PbO vs. MnO contents in weight percent (%) of the analyzed goethites in samples CO-102 and CO-79. The data regarding sample CO-79 refers exclusively to acicular goethites.

$$MnO_{2(s)} + 4H^{+}{}_{(aq)} + e^{-} \leftrightarrow Mn^{3+}{}_{(aq)} + 2H_2O_{(l)}, E^0 = 0.95\ \text{v} \quad (4)$$

where all E^0 values were taken from Bard et al. (1985). From the observation of both half-reactions, it becomes obvious that oxidation of Fe and reduction of Mn is promoted at acidic pH conditions. While it is difficult to speculate on the presence of Mn^{2+} in solution at such stage, Luo et al. (2018) demonstrated that aqueous Mn^{2+} does not affect the formed iron oxide species but increases the oxidation rate of Fe^{2+}. Since Mn^{3+} is the most relevant species to the nucleation of both layered and tunnel-manganese oxides, such species is at the center of our discussion. In this framework, it is possible to postulate that the extension of goethite dissolution is a major controlling factor behind the ratio of Mn^{3+}/Mn^{4+} in solution, which in turn influences the saturation state with respect to different types of Mn oxides. For instance, as deduced from the present data alongside with the determinations of Post et al. (2020), hollandite-group solid solution members comprise manganese in both oxidation states with varying proportions, to neutralize cationic contents of structural tunnel sites. In sample CO-79, corresponding to a higher enrichment in Mn oxides, most of the mineralogical content relates to intergrown acicular goethite and manganite (MnOOH), where all manganese is in 3+ oxidation state. Such textural relationship arises from the following reaction:

$$MnO_{2(s)} + Fe^{2+}{}_{(aq)} + 2H_2O_{(l)} \leftrightarrow Mn(OH)_{3(s)} + Fe(OH)_{3(s)} + 2H_2O_{(l)} + 2H+{}_{(aq)} \quad (5)$$

Since both $Fe(OH)_3$ and $Mn(OH)_3$ are unstable, they readily form goethite and manganite by dehydration (Betechtin, 1971). A striking feature from the described reactions is the increase in acidity as a by-product of the precipitation of $Mn(OH)_3$, which will necessary back-feed further dissolution of goethite, and the formation of more manganite following the acidic reduction expressed by half-reaction (4). The occurrence of both massive and acicular manganite seems to support such mechanism of continuous mineralogical transformation. In fact, a similar process for mobilizing and re-precipitating vast amounts of both manganese and iron was proposed by Pracejus et al. (1988), in its seminal work about the Mn sedimentary ores of Groote Eylandt. It is worth noting that lower valence Mn minerals are passive under the reducing conditions and become concentrated as higher valence oxides are leached away (Pracejus et al., 1988). The absence of manganite in sample CO-102, where the predominant Mn-phase is coronadite, may be explained by a concentration of aqueous Mn^{3+} insufficient to reach saturation with respect to manganite. Such also equates to the occurrence of less reductive conditions leading to the formation of coronadite ($Mn^{3+}/Mn^{4+} = 0.35$) in sample CO-102.

In sample CO-79, the occurrence of ramsdellite (MnO_2) lining the walls of fractures and cavities suggests the precipitation of Mn oxide under oxidative conditions, after the formation of manganite. Fig. 8 displays a micrograph of a cavity in sample CO-79, connected to a complex network of fractures, which enabled the reactive circulation of fluids. The shown chemical profile across the cavity-bearing vein, regarding contents in Mn, Ba, Zn and K, together with the acquired Raman spectra, enabled identifying the several Mn oxide phases present in a sequence of layers. The drusy growths from fracture walls clearly indicates that the crystallization sequence progressed inwards, towards the cavity, following the order ramsdellite, cryptomelane, and chalcophanite, this last in geodes. Focusing on the oxidation state of manganese in the structure of each phase, the initial conditions clearly progressed from oxidative, promoting the precipitation of $Mn^{4+}O_2$, to more reducing conditions, yielding the precipitation of cryptomelane, where Mn^{3+}/Mn^{4+} corresponds to approximately 0.16. Furthermore, aqueous cationic content supplied the necessary species for tunnel structural sites. Growth of chalcophanite as geodes of prismatic crystals in cavities indicates nucleation and growth from an isolated, static fluid.

The earlier precipitation of Mn in other phases and the isolation of the aqueous phase from the surrounding media, favored the crystallization of a structurally layered manganese oxide with lower ratios of Mn with respect to other cations in tunnel or interlayer structural sites (7:1 in hollandite group minerals, 3:1 in layered Mn oxides). However, the texture seems to suggest a paradoxical combination of an acidic fluid with low fO_2 coexisting with a manganese oxide phase where all octahedral Mn is in +4 oxidation state. It is worth noting that chalcophanite is a Zn^{2+}-rich mineral and Maithreepala and Doong (2004) found that such cation displayed an inhibitory effect over the reductive reactivity of Fe^{2+}-treated goethite towards Mn. Furthermore, the lack of a continuous supply of aqueous electron donors in a static, isolated fluid may have favored the nucleation of a phase where all manganese in octahedral sites is in 4+ oxidation state. In the present work, however, we found that a small excess of Mn may be present in interlayer sites as Mn^{2+}. Fig. 9 depicts a sequential schematic representation of the reactive pathway leading to the paragenetic associations preserved in both samples CO-102 and 79.

6. Conclusions

The present research intended to apply Raman spectroscopy and

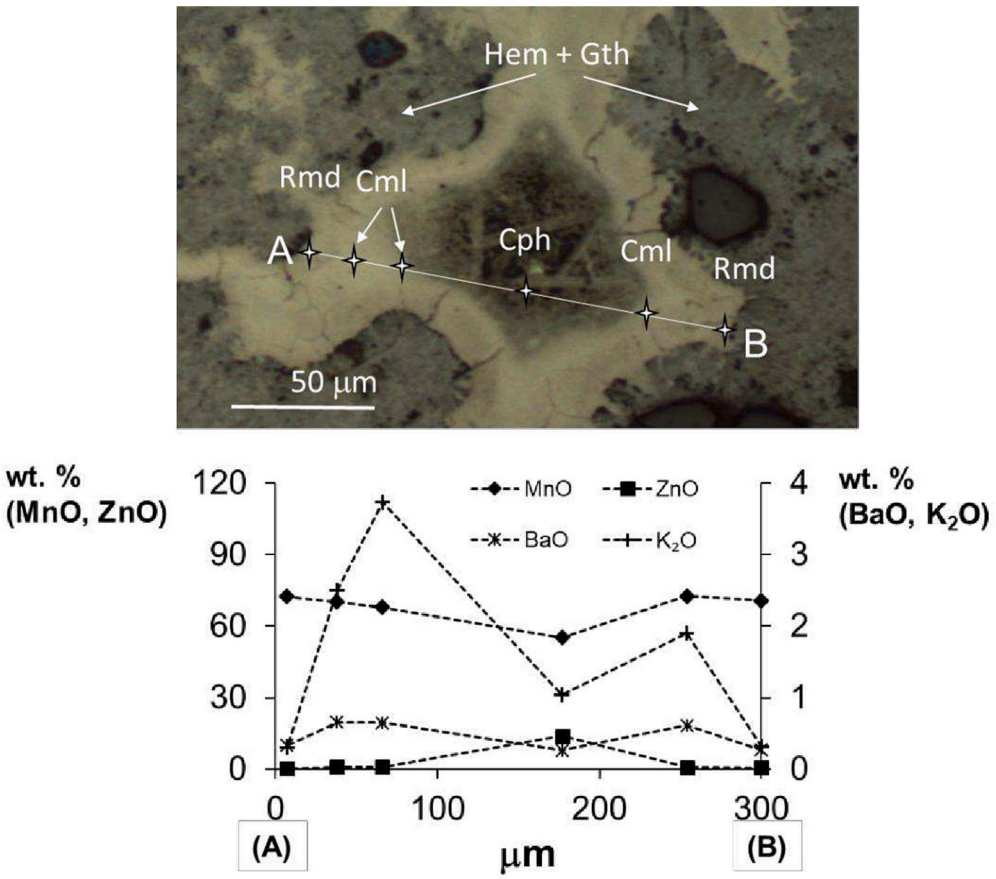

Fig. 8. Compositional profile (wt% MnO, ZnO, BaO and K_2O) across a cavity-bearing Mn-oxide vein in sample CO-79. Rmd = Ramsdellite, Cml = Cryptomelane, Cph = Chalcophanite, Hem = Hematite, Gth = Goethite.

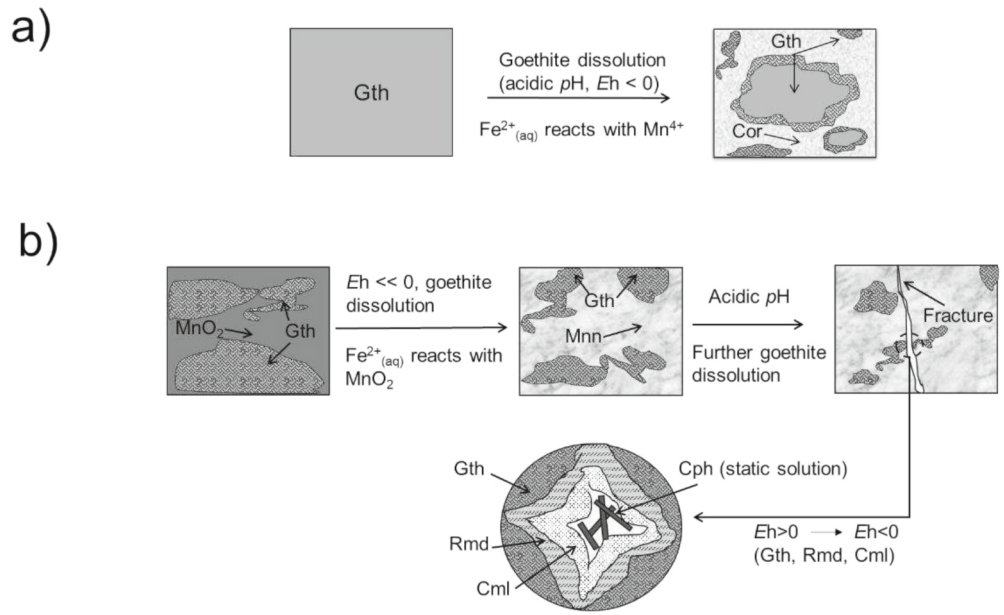

Fig. 9. Development of the paragenetic associations preserved in sample a) CO-102, and b) CO-79. The full explanation of the mineralization sequence is included in the text of Section 5.2. Gth = Goethite, Mnn = Manganite, Rmd = Ramsdellite, Cph = Chalcophanite.

EMPA analysis, to both the characterization and textural investigation of co-genetic, naturally occurring Mn oxides. From our research, focusing on samples from two different sections of the enriched zone of Serra da Mina Manganese Deposit, Portugal, it is possible to not only identify the several coexisting Fe and Mn phases, but also unravel the reactive pathways leading to supergene enrichment mineralizations. Namely,

changes in Eh/*p*H conditions can destabilize Fe oxides, such as goethite, promoting the release of Fe^{2+} into solution, whose electrochemical interaction with Mn^{4+} leads to the formation of several types of Mn oxides, and secondary goethite. The wide variety of observed Mn oxides is clearly related to the ratio of aqueous Mn^{3+}/Mn^{4+}, alongside other prevalent cations to be incorporated into tunnel or interlayer structural sites, which may be also supplied by dissolved goethite.

Author contribution statement

AJP and NSP collected the presented EMP and μRaman data and wrote the main manuscript text. RSJ collected the studied specimens, developed all the initial petrographic descriptions, defining targets for analysis, and revised the final version of the manuscript.

Declaration of Competing Interest

The authors declare that they have no known competing financial interests or personal relationships that could have appeared to influence the work reported in this paper.

Data availability

The research data used to construct all graphical representations and tables can be downloaded from the public access repository EarthChem.org, under https://doi.org/10.26022/IEDA/112768.

Acknowledgements

The study of the samples by Raman spectroscopy and microprobe analysis was supported by the MINECO (Spain) under the project CGL2016-77138-C2-1-P. This work was funded by the Portuguese Fundação para a Ciência e a Tecnologia (FCT) I.P./MCTES through national funds (PIDDAC) – UIDB/50019/2020. We would like to acknowledge the constructive criticism and sound suggestions provided by an anonymous reviewer #2, which contributed greatly to improve the quality of the present work.

References

Almeida, J., 1945. Considerações a Propósito do Manganésio do Alentejo. In: Estudos, Notas e Trabalhos do Serviço de Fomento Mineiro, 1, pp. 1–2.
Bard, A.J., Parsons, B., Jordon, J. (Eds.), 1985. Standard Potentials in Aqueous Solutions. Dekker, New York.
Bernardini, S., Bellatreccia, F., Municchia, A.C., Ventura, G.D., Sodo, A., 2019. Raman spectra of natural manganese oxides. J. Raman Spectrosc. 1–16.
Betechtin, A.G., 1971. Lehrbuch der speziellen Mineralogie. VEB Deutscher Verlag ftir Grundstoffindustrie, Leipzig, (1971).
Carvalho, D., de Fe-Mn, Jazigos, Cercal-Odemira, Da Região, 1971. Principais Jazigos Minerais do Sul de Portugal. Livro-Guia 4, 65–73.
Clark, R.J.H., Curri, M.L., 1998. The identification by Raman microscopy and X-ray diffraction of iron-oxide pigments and of the red pigments found on Italian pottery fragments. J. Mol. Struct. 440, 105–111.
De Faria, D.L.A., Venâncio Silva, S., De Oliveira, M.T., 1997. Raman microspectroscopy of some iron oxides and oxyhydroxides. J. Raman Spectrosc. 28, 873–878.
Fateley, W.G., Dollish, F.R., McDevitt, N.T., Bentley, F.F., 1972. Infrared and Raman Selection Rules for Molecular and Lattice Vibrations: The Correlation Method. Wiley.
Gutzmer, J., Beukes, N.J., 2009. Iron and manganese ore deposits: Mineralogy, geochemistry and economic geology. In: De Vivo, B., Grasemann, B., Stüve, K. (Eds.), Geology, vol. IV. EOLSS Publishers/UNESCO, Oxford, pp. 43–69.
Hanesch, M., 2009. Raman spectroscopy of iron oxides and (oxy)hydroxides at low laser power and possible applications in environmental magnetic studies. Geophys. J. Int. 177, 941–948.
Hochella, M.F., Kasama, T., Putnis, A., Putnis, C.V., Moore, J.N., 2008. Environmentally important, poorly crystalline Fe/Mn hydrous oxides: ferrihydrite and possibly new vernadite-like mineral from the Clark Fork River Superfund Complex. Am. Mineral. 90, 718–714.
Huang, J., Zhang, H., 2020. Redox reactions of iron and manganese oxides in complex systems. Front. Environ. Sci. Eng. 14 (5), 76.
Luo, Y., Ding, J., Yougang, S., Wenfeng, Y., Guohong, Q., Liu, F., 2018. Symbiosis mechanism of iron and manganese oxides in oxic aqueous systems. Chem. Geol. 488, 162–170.
Maithreepala, R., Doong, R.A., 2004. Synergistic effect of copper ion on the reductive dechlorination of carbon tetrachloride by surface-bound Fe(II) associated with goethite. Environ. Sci. Technol. 38 (1), 260–268.
Malinenko, V.P., Aleshina, L.A., Pergament, A.L., Germak, G.V., 2013. Switching effects and metal−insulator transition in manganese oxide. J. Sel. T Nan-Elec. Comp. 1 (1), 44–49.
McBreen, J., 1975. The electrochemistry of β-MnO2 and γ-MnO2 in alkaline electrolyte. Elec. Chim. Act. 20 (3), 221–225.
Michailidis, K.M., Nicholson, K., Nimfopoulos, M.K., Patrick, R.A.D., 1997. An EPMA and SEM study of the Mn-oxide mineralization of Kato Nevrokopi, Macedonia, Northern Greece: controls on the formation of the Mn^{4+} oxides. Geol. Soc. Lond. 119, 265–280.
Oh, S.J., Cook, D.C., Townsend, H.E., 1998. Characterizasion of iron oxides commonly found as corrosion products of steel. Hyperfine Interact. 112, 59–65.
Post, J.E., Appleman, D.E., 1988. Chalcophanite, $ZnMn_3O_7{\cdot}3H_2O$: new crystal structure determinations. Am. Mineral. 73, 1401–1404.
Post, J.E., McKeown, D.A., Heaney, P.J., 2020. Raman spectroscopy study of manganese oxides: tunnel sctructures. Am. Mineral. 105, 1175–1190.
Post, J.E., McKeown, D.A., Heaney, P.J., 2021. Raman spectroscopy study of manganese oxides: layer structures. Am. Mineral. 106, 351–366.
Pracejus, B., Bolton, B.R., Frakes, L.A., 1988. Nature abd development of supergene manganese deposits, Groote Eylandt, Northern Territory, Australia. Ore Geol. Rev. 4, 71–98.
Rout, K., Dash, A., Mohapatra, M., Anand, S., 2014. Manganese-doped goethite: structural, optical and adsorption properties. J. Ev. Chem. Eng. 2 (1), 434–443.
Roy, S., 1981. Manganese Deposits. Academic Press, London, 458 pp.
Santelli, C.M., Webb, S.M., Dohnalkova, A.C., Hansel, C.M., 2011. Diversity of Mn oxides produced by Mn (II)-oxidizing fungi. Geochim. Cosmochim. Acta 75, 2762–2776.
Santos, R., 2020. Caracterização Mineralógica, Petrográfica e Geoquímica das Mineralizações Ferro-Manganesíferas da Toca do Mocho/ Serra da Mina (Faixa Piritosa Ibérica). University of Lisbon, Faculty of Sciences unpublished MSc. Thesis.
Singh, R., Meenaloshini, S., 2008. Effect of manganese oxide on the sintered properties and low temperature degradation of Y-TZP ceramics. Ceram. Int. 34 (7), 1603–1608.
Taujale, S., Baratta, L.R., Huang, J., Zhang, H., 2016. Interactions in ternary mixtures of MnO_2, Al_2O_3, and natural organic matter (NOM) and the impact on MnO_2 oxidative reactivity. Environ. Sci. Technol. 50 (5), 2345–2353.
Tebo, B.M., Bargar, J.R., Clement, B.G., Dick, G.J., Murray, K.J., Parker, D., Verity, R., Webb, S.M., 2004. Biogenic manganese oxides: properties and mechanisms of formation. An Rev. Eart Plan. Sci. 32, 287–328.
Wojdyr, M., 2010. Fityk: a general-purpose peak fitting program. J. Appl. Crystallogr. 43, 1126–1128.
Zhao, W., Liu, F., Feng, X.H., Tan, W.F., Qiu, G.H., Chen, X., 2012. Fourier transform infrared spectroscopy study of acid birnessites before and after Pb^{2+} adsorption. Clay Miner. 47, 191–204.